



Development of a portable laser-flash photolysis Faraday rotation spectrometer for measuring atmospheric total OH reactivity

Bo Fang¹, Nana Wei¹, Weixiong Zhao¹, Nana Yang¹, Hao Zhou¹, Heng Zhang^{1,2}, Jiarong Li¹, Weijun Zhang¹, Yanyu Lu^{3,4}, Zhu Zhu^{4,5}, Yue Liu^{4,5}

5 ¹Laboratory of Atmospheric Physico-Chemistry, Anhui Institute of Optics and Fine Mechanics, HFIPS, Chinese Academy of Sciences, Hefei 230031, Anhui, China

²Institutes of Physical Science and Information Technology, Anhui University, Hefei 230039, Anhui, China

³Anhui Institute of Meteorological Sciences, Anhui Province Key Laboratory of Atmospheric Science and Satellite Remote Sensing, Hefei 230031, Anhui, China

10 ⁴Shouxian National Climatology Observatory, Huaihe River Basin Typical Farm Eco-meteorological Experiment Field of CMA, Shouxian 232200, Anhui, China

⁵Anhui Shouxian Meteorological Bureau, Shouxian 232200, Anhui, China

Correspondence to: Weixiong Zhao (wxzhao@aiofm.ac.cn), Weijun Zhang (wjzhang@aiofm.ac.cn)

Abstract. Quantitative measurements of atmospheric total OH reactivity (k_{OH}') provide crucial insights into atmospheric photochemistry. However, widespread application of total OH reactivity measurements is challenging due to insufficient equipment and the complexity of existing instrumentation. In this work, we report the development of a portable laser-flash photolysis Faraday rotation spectroscopy (LP-FRS) instrument for real-time and in-situ measurement of k_{OH}' . To achieve efficient overlapping between the pump and probe laser and realize a long effective absorption path length, thus enabling high sensitivity measurement, a specific Herriott-type pump-probe optical multi-pass cell was designed with an overlapping factor of up to 75.4%. The instrument's optical box dimensions were 130 cm × 40 cm × 35 cm. The obtained efficient absorption path was ~ 28.5 m in a base length of 77.2 cm. The k_{OH}' detection precisions of the LP-FRS instrument were 2.3 s⁻¹ and 1.0 s⁻¹ with averaging times of 60 s and 300 s, respectively. The k_{OH}' measurement uncertainty was evaluated to be within 2 s⁻¹. Field measurement was performed, and the difference between the measured k_{OH}' and the model simulated from the measured reactive species was analysed. The developed portable LP-FRS instrument extends the measurement methods of atmospheric total OH reactivity, and has certain advantages in cost, operation, and transportation, which will play an increasingly important role in future atmospheric chemistry research.

1 Introduction

The hydroxyl (OH) radical is the most important oxidant in the atmosphere during daytime. It initiates the oxidation of most natural and anthropogenic trace gaseous species, thereby dominates their atmospheric lifetime. Knowledge of tropospheric OH chemistry contributes to our understanding of air pollution and climate change (Lu et al., 2018; Nicely et al., 2018). However, due to the large number (10⁴ - 10⁵) of volatile organic compounds (VOCs) (Goldstein and Galbally, 2007), a comprehensive interpretation of the sink mechanisms of OH is extremely challenging.



Total OH reactivity (k_{OH}'), the inverse of the OH chemical lifetime (τ_{OH}), serves as an crucial parameter for estimating the total loss rate of OH due to all atmospheric OH reactants (Yang et al., 2016). It is defined as the sum of OH reactant concentrations ($[X]$) weighted by their reaction rate coefficient with OH (k_{OH+X}), which can be expressed as

$$k_{OH}' = \tau_{OH}^{-1} = \sum k_{OH+X_i} [X_i] \quad (1)$$

where X_i is the i -th reactant. Measurement of k_{OH}' provides a powerful tool for both field campaigns and laboratory studies in atmospheric photochemistry (Stone et al., 2012; Fuchs et al., 2013). The balance between OH production and loss rate provides additional information on the OH sources (Martinez, 2003; Hens et al., 2014). The difference between measured and calculated k_{OH}' can be used to estimate the contribution from individually measured species, the total missing reactivity, and the role of unknown VOCs (Di Carlo et al., 2004; Mao et al., 2010; Sinha et al., 2012). The measured total OH reactivity can also be used as the chemical closure of the reactive carbon budget (Hunter et al., 2017; Safieddine et al., 2017; Heald et al., 2020). In addition, k_{OH}' measurements help to estimate instantaneous production potential and production regime of ozone (Sinha et al., 2012; Li et al., 2021; Kohno et al., 2022; Li et al., 2022). Recently, the long-term trend of k_{OH}' has been proven to be a key atmospheric oxidation capacity parameter for the formulation of ozone (O_3) pollution mitigation strategy (Wang et al., 2023).

Several methods for OH reactivity measurement have been developed (Yang et al., 2016; Fuchs et al., 2017), which can be divided into three categories: the indirect method known as the comparative reactivity method (CRM) (Sinha et al., 2008); the semi-direct technique involving flow tube - chemical ionization mass spectrometry (FT-CIMS) (Muller et al., 2018); and the direct method, including flow tube - laser induced fluorescence (FT-LIF) (Kovacs and Brune, 2001; Mao et al., 2009; Ingham et al., 2009; Hansen et al., 2014) and laser-flash photolysis - laser induced fluorescence (LP-LIF) (Sadanaga et al., 2004; Lou et al., 2010; Parker et al., 2011; Stone et al., 2016).

The CRM indirectly determines k_{OH}' by the competitive kinetics for OH between a reference molecule not present in normal atmospheric condition (e.g., pyrrole) and all reactive atmospheric species in ambient air. Commercial proton-transfer-reaction mass-spectrometry (PTR-MS) or gas chromatography (GC) is employed to detect the concentration change of pyrrole (Nödscher et al., 2012). The direct method determined k_{OH}' from the measured time-dependent OH decay. The FT-LIF directly measures OH decay by controlling the reaction time through the movement of an OH injector along a flow tube. A LIF instrument is positioned downstream of the flow tube to monitor the OH concentration signal intensity. In LIF instrument, the sample is drawn into a low-pressure (~ 1.5 Torr) cell via gas expansion. A 308 nm dye laser is used to excite OH, and the resulting 308 nm fluorescence emitted by OH is collected for concentration evaluation. The LP-LIF is a pump-probe technique where OH decay can be observed with high time resolution after each flash without needing to determine the reaction time. In this technique, OH is produced by laser-flash photolysis of O_3 at 266 nm in the presence of water vapour, making it less susceptible to the recycling process caused by nitric oxide (NO) compared to the above instruments using water vapour photolysis (Sadanaga et al., 2004; Lou et al., 2010). In the semi-direct technique of FT-CIMS, sulphuric



65 acid (H_2SO_4) instead of OH is measured by a CIMS instrument to record the data point of OH decay at each reaction time. The reaction time can be varied by converting OH to H_2SO_4 at different fixed positions within the flow tube.

The instrument performances of the above techniques have been intercompared and validated in the simulation chamber SAPHIR, demonstrating that the direct methods offer advantages in detection precision and accuracy (Fuchs et al., 2017). However, the high cost of development and operation, limited instruments, complex operation and calibration procedures, and relatively large size of these instruments hinder the widespread application of measuring OH reactivity.

70 In this work, we report the development of a portable LP-FRS instrument for total OH reactivity measurement. The time-resolved laser-flash photolysis Faraday rotation spectroscopy (LP-FRS) is a novel technique that employs mid-infrared semiconductor diode laser as the probe laser for k_{OH} measurement (Wei et al., 2020). Since FRS relies on the detection of the probe light polarization state rotation induced by paramagnetic molecules in a longitudinal magnetic field, the laser noise and molecule interferences are significantly reduced, which enables the FRS system to directly, highly sensitive, and absolutely monitor the concentration of OH without any chemical interferences (Litfin et al., 1980; Zhao et al., 2018). The dimensions of the developed instrument were 130 cm \times 40 cm \times 35 cm. The achievable detection precision of k_{OH} was 1.0 s⁻¹ with 300 s averaging time. Field test in a suburban area was performed to demonstrate the capability of the LP-FRS instrument.

80 2 Experimental setup

A schematic diagram of the developed LP-FRS instrument is given in Fig.1(a). The instrument comprises a mid-infrared FRS system for direct measurement of OH and an ultraviolet (UV) laser-flash photolysis system for generating OH. The probe light and the UV beam have an overlapping in an Herriott-type optical multi-pass cell (MPC), enabling simultaneous monitoring of OH by the FRS system during the generation and reaction with reactants. Optical components from both systems are integrated into a single unitary box, with all communications and gas tubes connected to designated interfaces. The dimensions of the box are 130 cm \times 40 cm \times 35 cm, making the LP-FRS instrument portable for field applications.

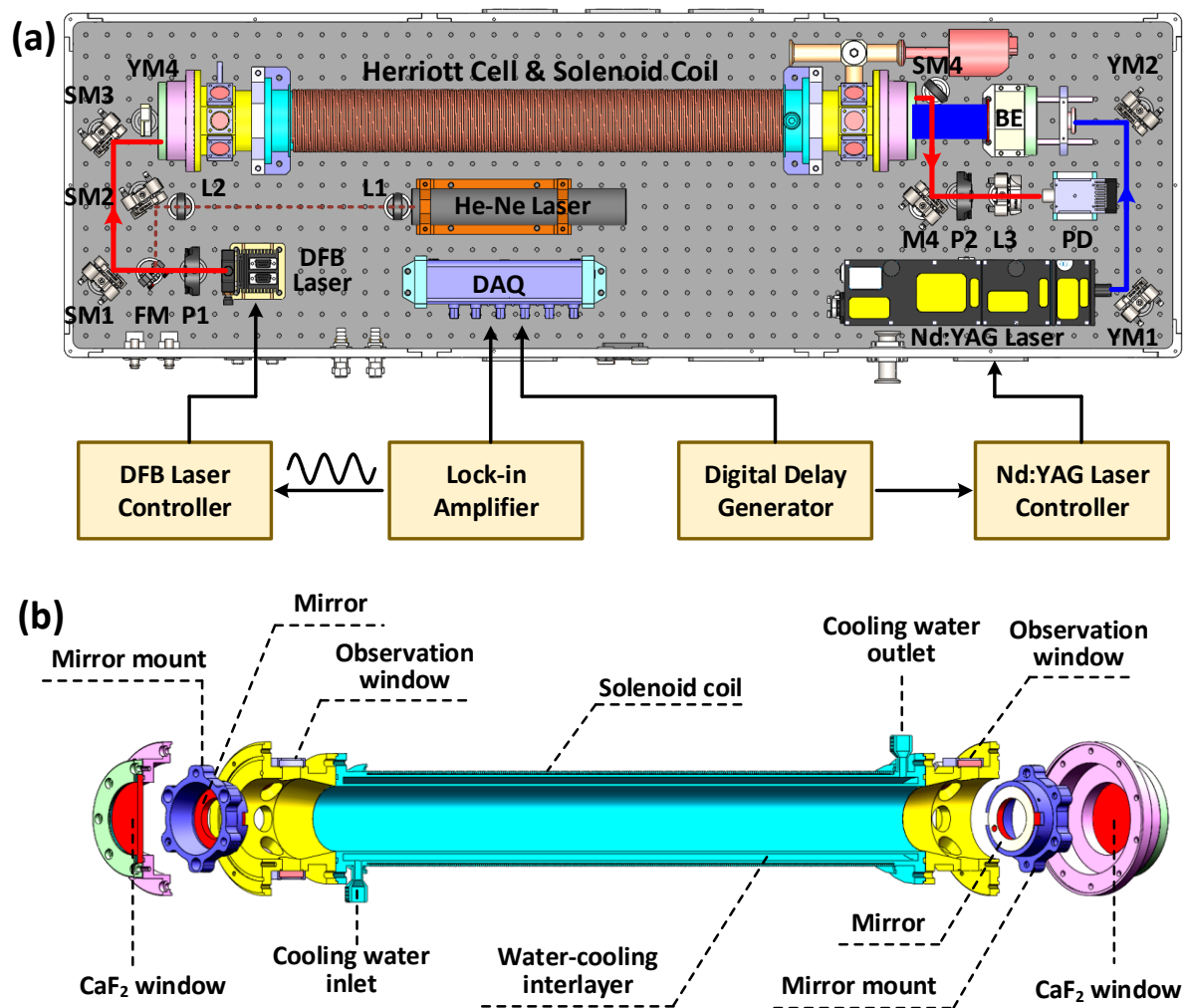


Figure 1: (a) Schematic diagram of the developed laser-flash photolysis Faraday rotation spectrometer (LP-FRS) which consists of a mid-infrared Faraday rotation spectroscopy system and a laser photolysis system. The OH radicals are generated by laser-flash photolysis at 266 nm in a Herriott cell wound with copper wires, and detected simultaneously by Faraday rotation spectroscopy via the overlapping mid-infrared optical paths. P, polarizer; FM, foldable mirror; SM, silver mirror; L, lens; PD, photodetector; YM, Nd: YAG mirror; BE, beam expander; DAQ, data acquisition card. (b) Assembly diagram of the Herriott-type pump-probe MPC. The coil is wound around the body of the MPC. A water-cooling interlayer is designed for temperature control of the solenoid coil and the cell.



2.1 Mid-infrared Faraday rotation spectrometer

A mid-infrared continuous wave distributed feedback laser (cw-DFB laser, Nanoplus GmbH) emitting at 2.8 μm is used as the probe laser. The current and temperature of the laser chip are controlled by a laser controller (LDC501, Stanford Research Systems). By changing the injection current from 90 to 130 mA at the operating temperature of 33 $^{\circ}\text{C}$, the wavelength of the DFB laser can be tuned from 3568.939 to 3568.362 cm^{-1} . The current tuning coefficient is about 0.0024 cm^{-1}/mA near the target Q(1.5e) line of the $^2\Pi_{3/2}$ state of OH at 3568.523 cm^{-1} . The selected line has the strongest line strength of $S = 9.032 \times 10^{-20} \text{ cm}^{-1}/(\text{molecule cm}^{-2})$ at 296 K (Gordon, et al., 2022) with the largest effective g_J value of 0.936 in the infrared region, which make it preferable for the FRS detection (Zhao et al., 2011; Zhao et al., 2012). The collimated beam output from the laser head passes through a Rochon prism (Foctek Photonics), with an extinction ratio of $\xi < 5 \times 10^{-6}$, to establish a linearly polarized state, and then incident into a Herriott-type pump-probe MPC. A He-Ne laser serves as an indicator. The beam waists of both lasers are aligned at the centre of the MPC to minimize beam divergence after each reflection (Pilgrim et al., 1997). A flipper optical mount facilitates switching between the two lasers. A second Rochon prism is placed at the output path to analyse the polarization state. The exited beam from the MPC is focused on a thermoelectrically cooled mercury cadmium telluride (MCT) photodetector (PVI-4TE-3.4, VIGO System). To effectively modulate the magnetic circular birefringence in a static magnetic field (Zhao et al., 2018; Fang et al., 2020; Wei et al., 2020), a 33 kHz sinusoidal wave from a lock-in amplifier (SR830, Stanford Research) is added to the laser injection current. The detector signal is processed by the lock-in amplifier to demodulated the second harmonic ($2f$) of the FRS signal. As the laser current is fixed at the absorption peak of the OH radical, time-resolved Faraday rotation spectrum that directly reflects the concentration variation of OH radical can be measured (Wei et al., 2020; Cheng et al., 2023).

The pump-probe MPC, as shown in Fig.1(b), consists of a cylindrical stainless steel tube with an inner diameter of 5 cm, a total length of approximately 89 cm, and a sample volume of 1.5 L. At both ends, a pair of 6.8 cm diameter calcium fluoride (CaF_2) windows are used for sealing and light transmission. Two gold-coated concave spherical mirrors, each 5 cm in diameter, are spaced 77.2 cm apart within the cell. Each mirror features a 5 mm diameter hole for probe light incidence and exit, and a central 32 mm diameter hole (i.e., the maximum diameter permissible for the UV beam passage) for the expanded photolysis beam. Mirror tilt and spacing are adjustable via three screws distributed circularly on the mirror mount. At each end of the MPC, there are eight circular quartz observation windows near the mirrors to facilitate multi-pass light adjustments. 25 reflection spots arrange on the mirror surfaces in a circular pattern with 2 cm radius. The total path length of the MPC is 37.8 m.

A solenoid coil, wrapped with 1 mm diameter red-copper enamelled wires, is wound around the stainless steel tube and operates in DC mode to offer a static magnetic field for FRS. The length and the outer diameter of the coil are 59 cm and 10 cm, respectively. The magnetic intensity tuning coefficient at the centre of the coil is 73 G/A. A water-cooling interlayer is designed for temperature control of both the solenoid coil and the cell.



2.2 Ultraviolet laser-flash photolysis system

130 A flashlamp pumped Nd: YAG laser (Big Sky Laser Ultra 100, Quantel) is employed as the photolysis laser. The laser wavelength is frequency doubled to generate the fourth harmonic radiation at 266 nm with pulse energy of 25 mJ, energy stability of ~ 2%, pulse length of ~ 6 ns, and beam diameter of ~ 4 mm. The water cooled laser head has a size of ~ 30.6 cm × 7.6 cm × 5.6 cm, and is controlled by an integrated cooling and electronics unit. The 266 nm pulse emitted from the laser head is directed coaxially into the MPC using two dielectrically coated 1-inch diameter mirrors. Prior to entering the cell, the diameter of the 266 nm beam is expanded to 32 mm using a beam expander consists of a quartz concave lens with a focal length of 12.5 mm and a quartz convex lens with a focal length of 100 mm.

135 A digital delay generator (DG645, Stanford Research Systems) was used to control the time sequence of laser-flash photolysis to record the time-resolved OH decay curve. The pump and Q-switch of the Nd: YAG laser are synchronized with two 4 Hz TTL (transistor-transistor logic) pulses delayed by 30 ms relative to the data acquisition to achieve the baseline of the OH decay curve. The rising edges of the pulses are used for triggering. The spectrum is sampled with 1000 data points, each separated by a time interval of 0.2 ms.

3 Instrument performance

3.1 Characterization of the pump-probe MPC

The MPC in the instrument determines the effective absorption path length of the FRS system for OH measurement (Wei et al., 2020; Yan et al., 2020). As shown in Fig.2(a), the mid-infrared light undergoes multiple passes between two mirrors within the MPC is used for OH detection; the expanded 266-nm UV pulse is employed for producing OH. The overlapping factor ($\eta = l/d$) can be defined as the ratio of the overlapping length (l) to the base length (d) of the MPC. For developing portable instruments, increasing the overlapping factor is crucial to achieve long effective path length while reducing the MPC base length. The Herriott-MPC in the developed LP-FRS instrument is specially designed with a small multi-pass light distribution circle radius at the centre to achieve a high overlapping factor. The radius of the multi-pass light distribution circle at the centre of the Herriott-MPC can be calculated with (Trutna and Byer, 1980):

$$r_c = r \left(\frac{g_1 + 2g_1g_2 + g_2}{4g_2} \right)^{1/2} \quad (2)$$

155 where g ($g = g_1 = g_2 = \cos \theta = 1 - d/R$) is the parameter that describes the optical resonance stability of optical cavity or MPC, θ is half of the angle between two adjacent reflection light points on mirror surface, $R_1 = R_2 = R$ is the curvature radii of the mirrors, r is the radius of the spot distribution circle.

Fig.2(b) illustrates the variations in r_c , g and η as functions of θ . When θ value is below than 79.2° , the r_c exceeds the 16 mm radius of the photolysis beam, resulting in no overlapping path. As the θ approaches -1 , the value of r_c decreases and the



160

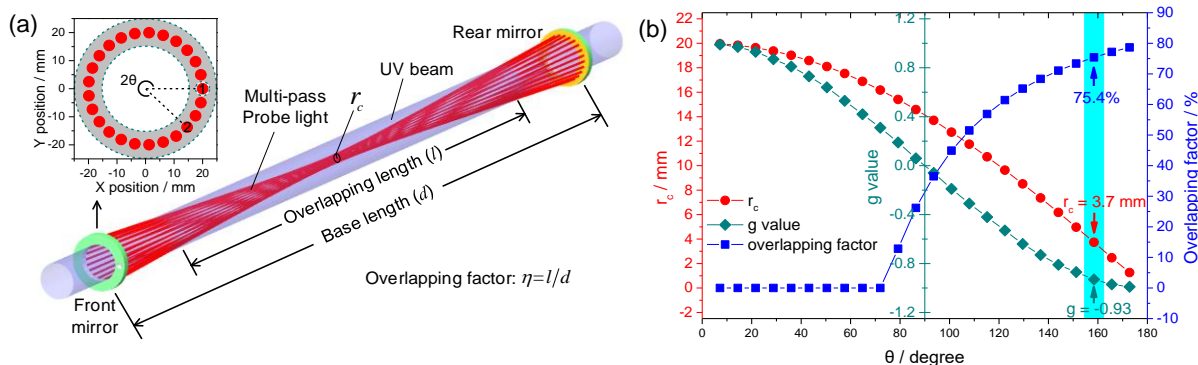


Figure 2: (a) Schematic of the Herriott multi-pass cell and the beam pattern on mirror surface for pump-probe; (b) multi-pass light waist (r_c), g value and overlapping factor (η) as functions of θ . θ is half of the angle between two adjacent reflection spots. The θ of 158.4° is selected, achieving an $r_c = 3.7$ mm and a η of 75.4%.

165

Table 1. Performance comparison of MPCs used for laser photolysis in pump-probe techniques.

MPC type	Base length (cm)	Effective overlapping path length (m)	Overlapping factor	References
Multi-pass arrangement	150	4.4	35.9%	Lewis et al., 2018
	150	7.0	41.9%	Lewis et al., 2018
Herriott cell	90	12	33.3%	Pilgrim et al., 1997
	125	45	64.0%	Pilgrim et al., 1997
	100	3.5	18.4%	Qian et al., 2000
	73	13	80.2%	Luo et al., 2019
	65.5	24.5	58.6%	Luo and Horng, 2020
	65.5	20.9	50%	Luo et al., 2020
	122	25	41.7%	Wei et al., 2020; Cheng et al., 2023
	91.3	6.3	32.9%	Yan et al., 2020; Teng et al., 2021
	77.2	28.5	75.4%	This work



A comparison of effective overlapping path lengths and overlapping factors with literature reported MPCs used in pump-probe techniques is shown in Table 1. The effective overlapping path length of these MPCs ranged from sever meters to tens
 170 of meters with base lengths around 100 cm (Pilgrim et al., 1997; Luo et al., 2019; Qian et al., 2000; Lewis et al., 2018; Luo and Horng, 2020; Luo, 2020; Wei et al., 2020; Yan et al., 2020; Teng et al., 2021; Cheng et al., 2023). The overlapping factor of our MPC was comparable to that developed by Lou et al., 2019, for a similar base length, while our effective overlapping path length was twice as long.

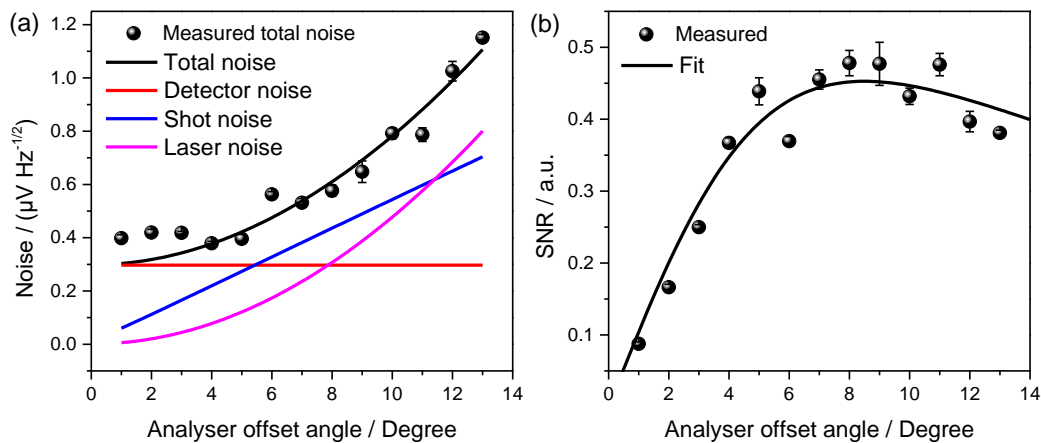
3.2 Optimization of the FRS system

175 For weak absorption, the FRS signal (S_{FRS}) and total noise (N_{tot}) of the system can be expressed as functions of the analyser offset angle (ϕ) from the crossed polarization of the light (Zhao et al., 2011; Wei et al., 2020):

$$S_{\text{FRS}}(\nu) = \gamma N S L P_0 \sin(2\phi) \chi(\nu) \quad (3)$$

$$N_{\text{tot}}(\phi) = \sqrt{N_0^2 + \left(N_1 \sqrt{(\sin^2(\phi) + \xi)}\right)^2 + \left(N_2 (\sin^2(\phi) + \xi)\right)^2} \quad (4)$$

where ν is the laser frequency, γ is the instrumentation factor, N is the OH concentration, S is the absorption line strength
 180 of OH, χ is Faraday rotation lineshape (Westberg and Axner, 2014). N_0 , $N_1 \sqrt{(\sin^2(\phi) + \xi)}$ and $N_2 (\sin^2(\phi) + \xi)$ are the detector noise, shot noise and laser noise of the system, respectively. It is noted that FRS signal reaches its maximum value when $\phi = \pm 45^\circ$, while the total noise is more sensitive to $\sin^2(\phi)$. The maximum signal-to-noise ratio (SNR) usually occurs at a small offset angle, which depends on system noise (Lewicki et al., 2009).



185

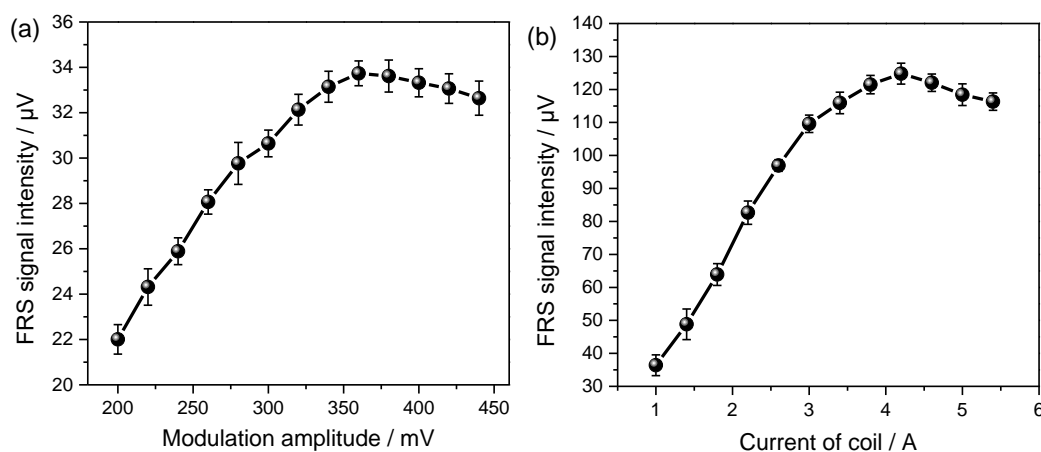
Figure 3: (a) Noise and (b) signal-to-noise ratio analysis of the FRS system. The optimum offset angle of analyser is 8° .

The total noises at various offset angles and the detector noise were measured with the lock-in amplifier to determine the noise sources and the optimum angle (ϕ_{opt}) for maximizing the SNR of the FRS system (Zhao et al., 2011). Fig.3(a) shows a



190 fit analysis of the data using Eq.(4). For offset angles below 5.5° , detector noise is the main noise of the system. The measured detector noise was $0.30 \mu\text{V Hz}^{-1/2}$ which closely agreed with the manufacturer's specified value of $290 \text{ nV Hz}^{-1/2}$. Laser noise dominates and rapidly increased beyond an offset angle greater of 11.5° . Since FRS signal is proportional to $\sin(2\phi)$, the relative SNR for a given absorption at a fixed laser frequency can be evaluated from $\text{SNR} \propto \sin(2\phi) / N_{\text{tot}}$. As shown in Fig.3(b), the SNR of our system peaks at the ϕ_{opt} of $\sim 8^\circ$. At this angle, the laser noise was suppressed to $0.31 \mu\text{V Hz}^{-1/2}$, equivalent to the detector noise level. The total system noise was $0.61 \mu\text{V Hz}^{-1/2}$ which was 1.4 times higher than the measured shot noise of $0.44 \mu\text{V Hz}^{-1/2}$.
195

In this work, the magnetic circular birefringence of OH was effectively modulated with wavelength modulation in a static magnetic field generated by the DC coil. The modulation amplitude and magnetic field strength are critical parameters that affecting the intensity of the demodulated FRS signal (Zhao et al., 2018; Fang et al., 2020). The theoretical optimum modulation amplitude is 2.2 times of the HWHM (half width at half-maximum) of the absorption lineshape (Schilt et al., 2003). The optimum magnetic field strength (B_{opt}) is the value that can make the Zeeman splitting comparable with the HWHM (Brecha et al., 1997). A direct and effective approach for determine the two optimum parameters is recording the signal intensity values under series amplitudes of the sinusoidal wave output from the lock-in amplifier and different coil currents. As shown in Fig.4, the FRS signal intensity value is calculated from the difference before and after laser-flash. The maximum intensity occurred at an amplitude of 360 mV and a coil current of 4.2 A, which corresponding to a wavelength modulation amplitude of $\sim 0.048 \text{ cm}^{-1}$ (~ 2.45 times of the calculated OH absorption linewidth of $\sim 0.020 \text{ cm}^{-1}$ in air) and a B_{opt} of 307 Gauss, respectively.
205

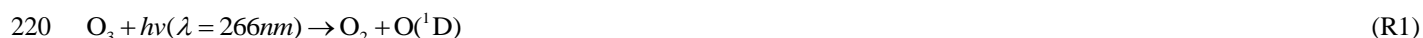


210 **Figure 4:** FRS signal intensity as functions of (a) modulation amplitude and (b) current of coil. The optimum modulation amplitude and magnetic field strength are 360 mV_{rms} and 307 Gauss, respectively.



3.3 OH concentration in the cell

To produce sufficient OH in the MPC, a small flow rate (~ 0.25 L/min) of zero air which passed through a UV lamp and a bubbling bottle to generate O_3 and water vapour, is added to the main sampling flow (~ 6.0 L/min), resulting in a total flow rate of 6.25 L/min. The operation pressure in the MPC is set to 200 mbar, and maintained by a butterfly valve (DN40, VAT). The flow velocity in the cell is 27 cm/s, corresponding to a Reynolds number of ~ 170 , which met the laminar flow condition. OH is produced by the 266 nm laser photolysis of O_3 , then followed by reaction of $O(^1D)$ with water vapour (Sadanaga et al., 2004):



The concentrations of O_3 and the water vapour directly influence the OH producing. A dewpoint sensor was used to measure the water vapour mixing ratio of the total flow. Based on Magnus-Tetens formula (Lawrence, 2005), the absolute water vapour mass concentration can be evaluated from $\rho(H_2O) = e/(R_w \cdot T)$, where $R_w = 461.52$ J/(kg K), T is the sample temperature, $e = C \times 10^{(A \cdot T_d / (B + T_d))} \cdot (P / P_0)$ is the actual water vapour pressure at current pressure of P , $A = 17.625$, $B = 243.04$ °C, $C = 610.94$ Pa, P_0 is the standard atmospheric pressure, T_d is the measured dewpoint temperature. The calculated water vapour volume concentration was $\sim 0.13\%$ when using zero air for system test, while it increased to $\sim 1.5\%$ when measuring real atmosphere. The O_3 concentration is estimated by measuring the energy of the photolysis laser pulse with the UV lamp on and off. Only about 0.3% of the pulse energy was absorbed by O_3 . Based on the Beer-Lambert law and the O_3 absorption cross section of $\sigma = 9.65 \times 10^{-18}$ cm² at 266 nm (Sadanaga et al., 2004), the O_3 concentration is determined to be ~ 800 ppbv. The recommended quantum yield of the $O(^1D)$ produced by laser flash photolysis is ~ 0.9 (Atkinson et al., 2004), resulting in $\sim 2.2 \times 10^{11}$ molecule/cm³ of $O(^1D)$. The number density of OH produced by the $O(^1D)$ can be estimated by (Wei et al., 2020):

$$[OH] = \frac{2k_6[O(^1D)][H_2O]}{(k_5[M] + k_6[H_2O])[O(^1D)]} \cong \frac{2k_6}{k_5} \chi_{H_2O} \quad (5)$$

where $[OH]$, $[O(^1D)]$, $[H_2O]$ and $[M]$ represent the number densities of the corresponding molecule. M is the “bath” gas during the chemical reaction of OH formation. χ_{H_2O} is the volume concentration of water vapour. k_5 and k_6 are 2.9×10^{-11} cm³ molecule⁻¹ s⁻¹ and 2.2×10^{-10} cm³ molecule⁻¹ s⁻¹ at 298 K, respectively. The concentration of OH produced in the cell was $\sim 4.3 \times 10^9$ molecule/cm³ during system test and was $\sim 5 \times 10^{10}$ molecule/cm³ during field application due to different χ_{H_2O} in the sample.

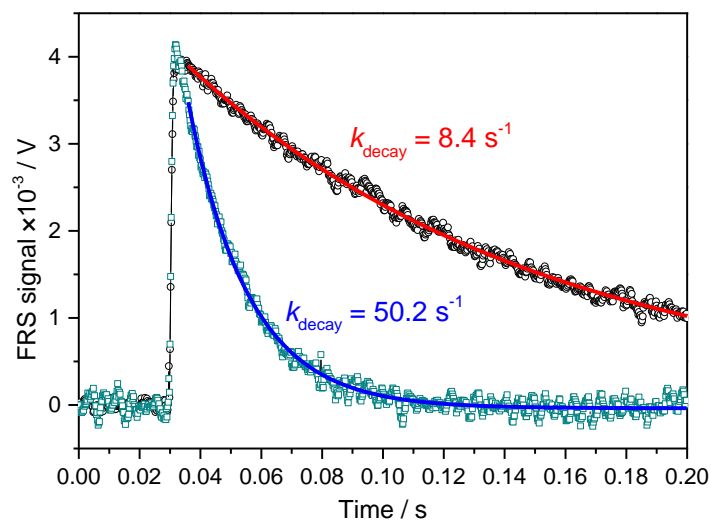


240 3.4 Kinetics test

The performance of the LP-FRS instrument in measuring different reaction rates were verified with three well-known reactions (Wei et al., 2020; Yan et al., 2020). Reactants from the cylinders (i.e., CH₄ (99.999%, Nanjingteqi), CO (2.01%, Nanjingteqi) and NO (100 ppmv, Linde)) were added to the main flow at different flow rates. When the concentrations of reactants are much higher than that of OH, the OH decay rate (k_{decay}) follows pseudo-first order kinetics and can be
245 determined by fitting the measured decay spectra to the flowing exponential equation:

$$y = a + b \exp(-k_{\text{decay}} t) \quad (6)$$

where y is the FRS signal intensity at the reaction time t . a and b are parameters representing the background signal intensity and the initial OH concentration, respectively. Since the fitted values for y and k_{decay} do not depend on the selected time period of the decay curve (Stone et al., 2016), the fit is started at the 180th data point rather than the peak to avoid any
250 fluctuations affecting the fitting result. Fig.5 shows two typical decays with loss rates of $k_{\text{decay}} = 8.4 \text{ s}^{-1}$ and $k_{\text{decay}} = 50.2 \text{ s}^{-1}$ which are given with 60 s averaging time during the measurements. The recorded time-resolved decay spectra clearly depict the entire event including the baseline, the instant generation of OH by laser photolysis, and the decay process.



255 **Figure 5:** Two typical OH decay spectra with different loss rates. Time zero is defined as the moment when the data acquisition trigger occurs.

The OH decay rates in the reactions with three different species were measured. As shown in Fig.6, the reaction rate constants for OH + CH₄, OH + CO, and OH + NO at 298 K, obtained from the slope of linear fittings between the decay rates and the concentrations, were found to be $k_{\text{OH}+\text{CH}_4} = 6.4 \times 10^{-15} \text{ cm}^3 \text{ molecule}^{-1} \text{ s}^{-1}$, $k_{\text{OH}+\text{CO}} = 1.6 \times 10^{-13} \text{ cm}^3 \text{ molecule}^{-1} \text{ s}^{-1}$,
260 and $k_{\text{OH}+\text{NO}} = 3.0 \times 10^{-12} \text{ cm}^3 \text{ molecule}^{-1} \text{ s}^{-1}$. The slope errors of the fittings were less than 0.1. The measured reaction rate



265

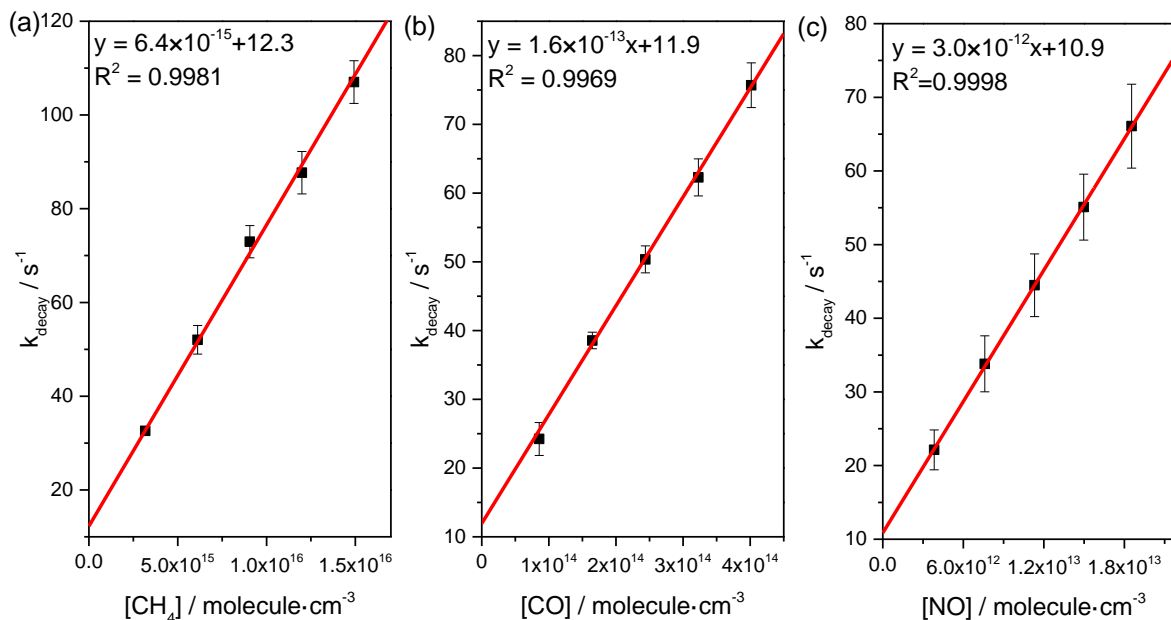


Figure 6: Plots of the measured pseudo-first-order rate coefficients vs (a) CH_4 concentrations, (b) CO concentrations and (c) NO at 298 K. The measured reaction rate constants are $k_{\text{OH}+\text{CH}_4} = 6.4(\pm 0.1) \times 10^{-15} \text{ cm}^3 \text{ s}^{-1}$, $k_{\text{OH}+\text{CO}} = 1.6(\pm 0.1) \times 10^{-13} \text{ cm}^3 \text{ s}^{-1}$, and $k_{\text{OH}+\text{NO}} = 3.0(\pm 0.1) \times 10^{-12} \text{ cm}^3 \text{ s}^{-1}$, which respectively agree with the recommend values.

270

3.5 Precision and uncertainty of $k_{\text{OH}'}$ measurement

When the LP-FRS instrument is used for measuring atmospheric $k_{\text{OH}'}$, the fitted k_{decay} value requires corrections for dilution and instrument zero (k_{zero}). Incorporating these corrections, the atmospheric $k_{\text{OH}'}$ is expressed as

$$k'_{\text{OH}} = f \times (k_{\text{decay}} - k_{\text{zero}}) \quad (7)$$

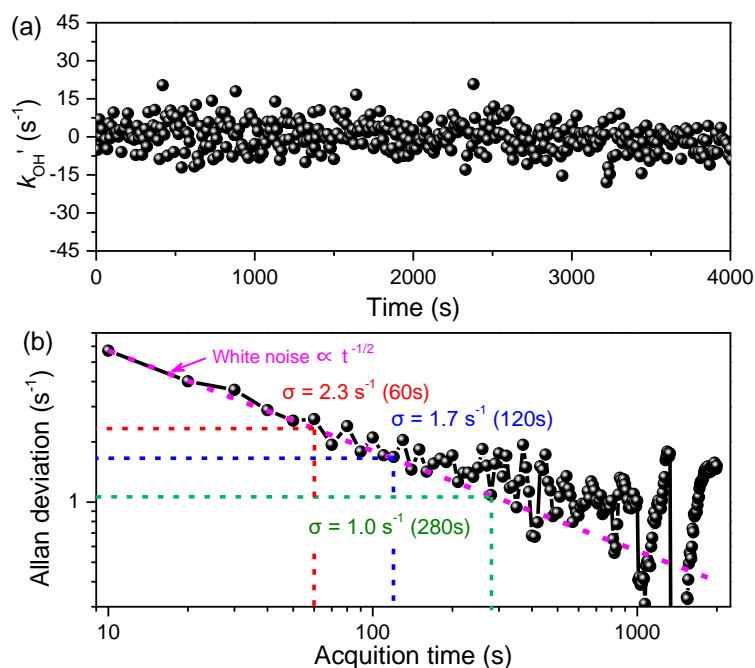
275 where f , given by $f = f_{\text{pressure}} \times f_{\text{flow}}$, is the total dilution factor which arises from the low operating pressure of 200 mbar and the additional small flow of humidified air containing a constant mixing ratio of O_3 . f_{pressure} represents the pressure dilution factor given by the ratio of the ambient pressure to the operation pressure, equal to ~ 5 . f_{flow} is the flow dilution factor calculated as the ratio of the total flow rate of 6.25 L/min to the sample flow rate of 6.0 L/min, equal to 1.04. Therefore, the total correction factor (f) is 5.2.



280 The instrument zero is critical for calculating $k_{\text{OH}'}$ from the observed OH decay rate and is usually assumed constant over
 a certain observation period. To evaluate instrument zero, OH decays rates were measured in zero air produced by a portable
 zero gas generator, yielding the k_{zero} of 5.2 s^{-1} . Several factors affect the instrument zero, including the self-reaction of OH,
 reaction of OH with O_3 , OH diffusion, and reaction of OH with residual reactive species in zero air. The self-reaction rate
 constant of OH is $1.48 \times 10^{-12} \text{ cm}^3 \text{ molecule}^{-1} \text{ s}^{-1}$ at 298 K (Atkinson et al., 2004), contributing to $\sim 1.5\%$ of the instrument
 285 zero at current OH concentration. The reaction rate constant of OH with O_3 is $7.3 \times 10^{-14} \text{ cm}^3 \text{ molecule}^{-1} \text{ s}^{-1}$ at 298 K
 (Atkinson et al., 2004), leading to an OH loss rate of 0.3 s^{-1} , which accounts for $\sim 6\%$ of the instrument zero. The OH loss
 rate due to diffusion (k_{dif}) under laminar flow condition can be calculated from (Ivanov et al., 2007; Liu et al., 2009):

$$k_{\text{dif}} = K_{\text{dif}} \times \frac{D_{\text{OH}}}{r_{\text{tube}}^2} \quad (8)$$

where $K_{\text{dif}}=3.66$ (for a cylinder cell) is the dimensionless geometric parameter, r_{tube} is the radius of the cell, $D_{\text{OH}} = 1.3 \text{ cm}^2$
 290 s^{-1} is OH diffusion coefficient at 200 mbar and 298 K in air. The calculated OH diffusion loss rate was 0.8 s^{-1} , giving a
 contribution of $\sim 15\%$ of the instrument zero.

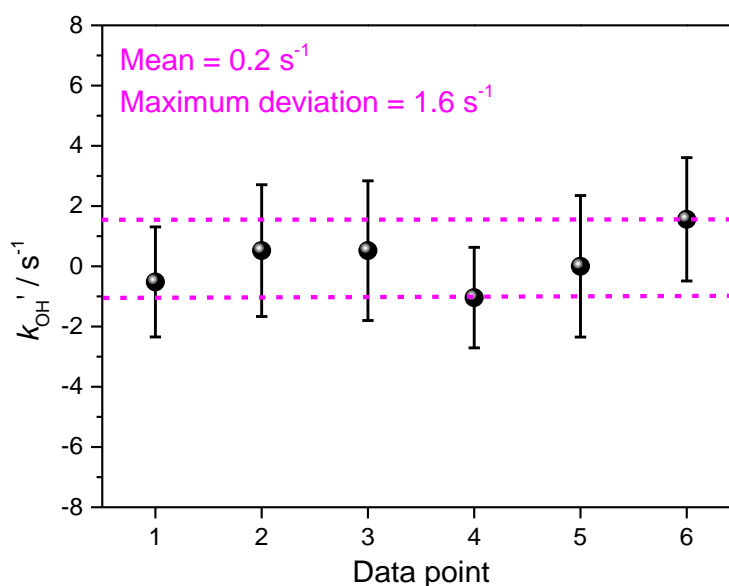


295 **Figure 7:** (a) Time series of zero air with 8 s time resolution and (b) the Allan deviation analysis of the time series. The
 measurement precision of $k_{\text{OH}'}$ can be improved to 2.3 s^{-1} and 1.0 s^{-1} with averaging times of 60 s and 300 s, respectively.



To assess the measurement precision of the LP-FRS instrument, an Allan deviation analysis was conducted on time series of zero air measurements. As shown in Fig.7, the averaging time of $k_{OH'}$ data point was 10 s with total a measurement
300 time of about 4000 s. The measurement precisions of $k_{OH'}$ were 2.3 s^{-1} and 1.7 s^{-1} with the acquisition time of 60 s and 120 s, respectively. When the averaging time increased to 300 s, the atmospheric $k_{OH'}$ measurement precision could further improved to 1.0 s^{-1} .

A comprehensive approach to evaluate the instrument's total uncertainty is measuring zero air. Fig.8 illustrates the $k_{OH'}$ values obtained from zero air on different days. Each value was obtained from a one-hour continuous measurements. The
305 time intervals for these zero value measurements are longer than two weeks. The error bars of the data points agreed well with the $k_{OH'}$ measurement precision obtained from Allan deviation analysis. No significant drift was found during measurements, with a mean value close to zero at 0.2 s^{-1} . The $k_{OH'}$ measurement uncertainty of the developed LP-FRS instrument, which can be determined from the deviations of these measurements, was within 2 s^{-1} . The uncertainty of the LP-FRS instrument arises from two main sources: the dilution factor and the instrument zero. The uncertainties associated with
310 the MFCs and the pressure controller used were $\sim 1\%$ and $< 1\%$, respectively, resulting in a total uncertainty of the dilution correction factor of less than 2%. The uncertainty of the instrument zero primarily originates from various influencing factors, such as changes in O_3 concentrations and residual reactants in zero air.



315 **Figure 8:** Measured $k_{OH'}$ values of zero air on different days. The total instrument uncertainty, determined from the measurements deviations, is within 2 s^{-1} .



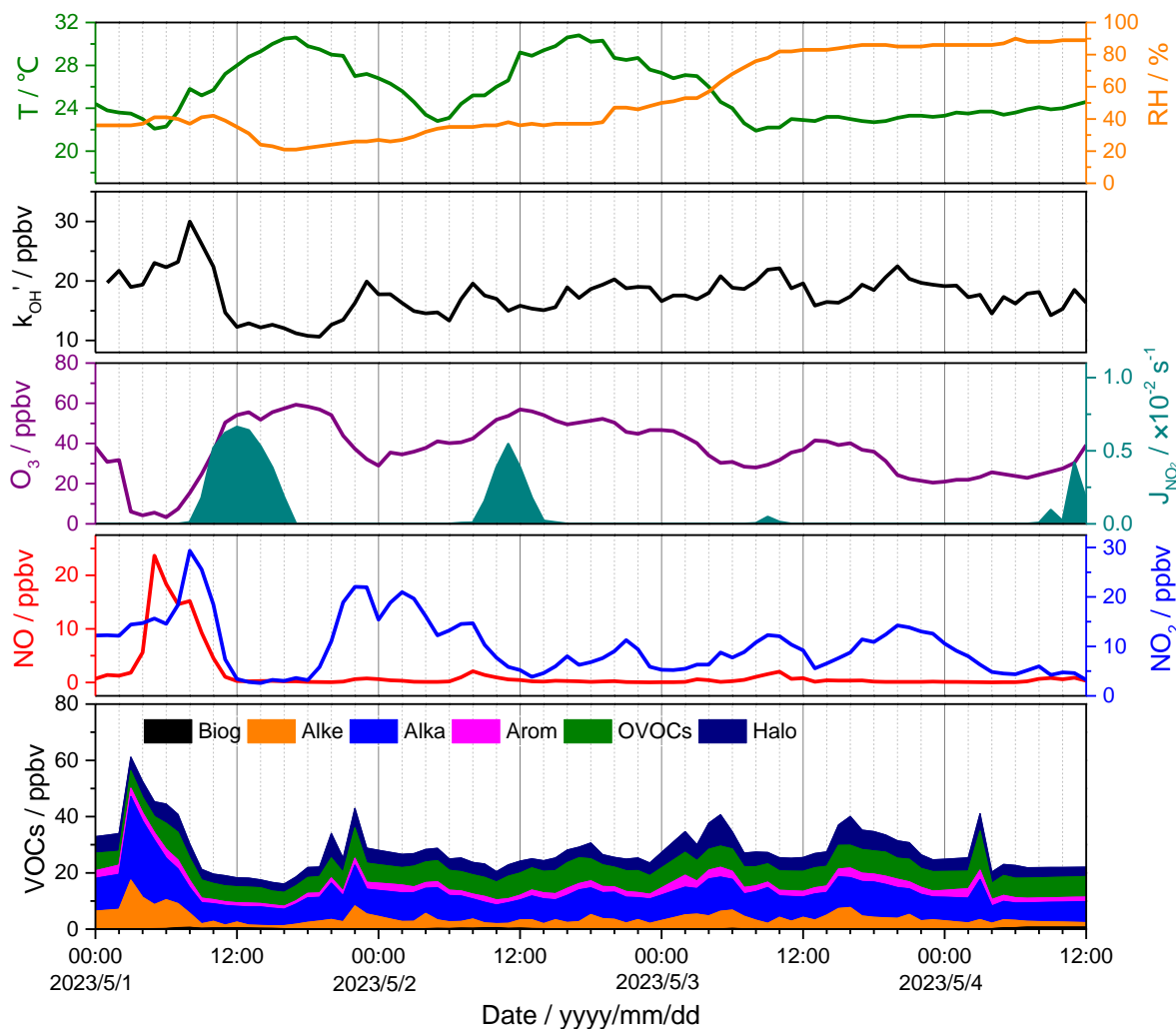
4 Field performance

The capability of the developed LP-FRS instrument was demonstrated through field measurements of atmospheric total OH reactivity. Measurements were conducted at the park of the Hefei Institutes of Physical Science, Chinese Academy of Sciences (31°91' N, 117°16' E) (Khayyam et al., 2024). This observation site is situated on a peninsula in a suburban area, surrounded by water on three sides. There were also an optical and several mechanical processing factories located on the peninsula. The observation period spanned from May 1st to May 4th, 2023.

The LP-FRS instrument was housed in a container with the sampling port positioned ~ 1.2 m above the container's roof. In addition to measuring OH reactivity, concentrations of 115 kinds of VOCs were analysed using a gas chromatograph coupled with a flame ionization detector and mass spectrometer (GC-FID/MS, TSQ9000, Thermo Fisher) with a time resolution of 1 hour. The VOCs included 29 alkanes (alka), 12 alkenes (alke), 16 aromatic hydrocarbons (arom), 35 halogenated hydrocarbons (halo), 21 oxygenated volatile organic compounds (OVOCs), 1 alkyne and 1 carbon disulfide. Concentrations of NO, NO₂ and O₃ were measured employing a NO_x analyser (42i, Thermo Fisher) and a O₃ analyzer (49i, Thermo Fisher). Data of ambient temperature (T) and relative humidity (RH) concentration were obtained from an automatic monitoring station located ~ 100 m from the container. Photolysis rate constant of J(NO₂) was measured with a photolysis spectrometer (PFS-100, Focus Photonics).

An overview of observed meteorological and gas concentrations is given in Fig.9. The average temperature and relative humidity during the observation period were 25.6 °C (range from 21.9 °C to 30.8°C) and 53.8% (range from 21% to 90%), respectively. The average concentrations of NO, NO₂ and O₃ were 1.5 ppbv, 10.0 ppbv and 36.7 ppbv, respectively. Alkanes, OVOCs and alkenes were the three VOCs with the highest concentrations during the field measurement period. The corresponding average concentrations were 9.7 ppbv, 7.1 ppbv and 3.8 ppbv, respectively. The measured BVOCs only include isoprene, with an average concentration of 0.2 ppbv. The minimum and maximum values of $k_{OH'}$ were 10.6 s⁻¹ and 30.0 s⁻¹, respectively.

The reactive species and $k_{OH'}$ exhibited distinct daily variations on May 1st (the first day of the International Labour Day holiday). The peak of VOC concentrations (60 ppbv) appeared at 3:00. The concentrations of NO began increasing significantly from 3:00 onwards, reaching a peak of 23.7 ppbv around 5:00. Concurrently, the abundant NO reacted with O₃, resulting in the lowest observed O₃ concentration (~ 5 ppbv) and an increase in NO₂ level. $k_{OH'}$ and NO₂ reached their peak values of 30.0 s⁻¹ and 29.3 ppbv at about 8:00 in the morning, declining rapidly as sunlight intensified, with the lowest values observed between 12:00 and 13:00. The highest O₃ concentration (59.3 ppbv) occurred around 17:00 in the afternoon. $k_{OH'}$ and species exhibited relatively low values in the following days, and no significant peak in NO concentration was observed in the afternoon. These changes could be attributed to “holiday effect” (Fatahi et al., 2021), which reflect the extensive vehicle travel on the eve and the first day of the holiday and decreased human activities near observation site during the holiday (Song et al., 2022).



350

Figure 9: Time series of observed meteorological and chemical parameters, including ambient temperature, relative humidity, total OH reactivity, photolysis frequencies ($J(\text{NO}_2)$), and concentrations of O_3 , NO , NO_2 and VOCs. The time period is from May 1st to May 4th, 2023.

355 A zero-dimensional box model (Framework for 0-Dimensional Atmospheric Modelling, F0AM) based on the Master Chemical Mechanism (MCM3.3.1) was applied for comparison with the observed total OH reactivity (Wolfe et al., 2016; Wei et al., 2023). The model was constrained by the measured species and parameters of meteorology and photolysis. Fig.10(a) shows the diurnal profiles of observed and simulated $k_{\text{OH}'}$. The observed $k_{\text{OH}'}$ ranged from 14.6 s^{-1} (at 14:00) to 21.9 s^{-1} (at 8:00) with an average value of 17.5 s^{-1} . According to pie chart analysis in Fig.10(b), inorganic species, alkenes, OVOCs and alkanes contributed 26.4%, 10.8%, 10.5% and 5.0% to the $k_{\text{OH}'}$, respectively. Contributions from aromatic and halogenated hydrocarbons were relatively low, accounting for 3.0% and 0.6%. The contribution of photochemical secondary

360



products (Others) was as high as 20.9%, while the missing reactivity (i. e., the difference between observed and simulated k_{OH}') averaged $\sim 20.5\%$, highlighting the significant role of photochemical and unidentified components in local atmospheric chemistry.

365

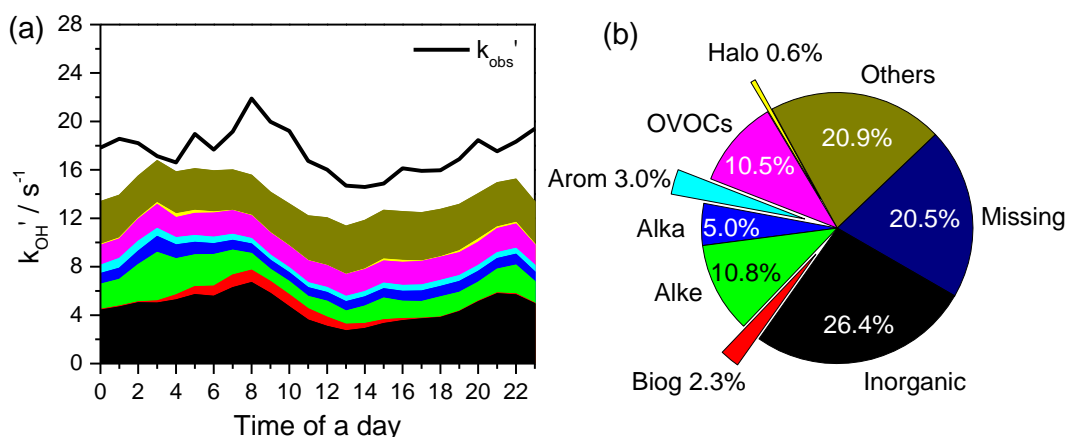


Figure 10: (a) Stack of diurnal profiles of observed k_{OH}' compared with calculated OH reactivity from individual groups of measured atmospheric species; (b) pie chart of contributions from each group to total reactivity.

370 5 Conclusions

A portable LP-FRS instrument was developed. A specific Herriott-type pump-probe MPC with a small multi-pass beam distribution circle radius of 3.7 mm at the centre of the cell was designed to offer an effective overlapping path length of ~ 28.4 m between the mid-infrared probe light and the photolysis light with a high overlapping factor of 75.4%. Such an overlapping factor benefit in reducing instrument size, resulting in dimensions of just 130 cm \times 40 cm \times 35 cm. The precision and uncertainty of the LP-FRS instrument for measuring atmospheric k_{OH}' were $1.0 s^{-1}$ (1σ , 300 s) and within $2 s^{-1}$, respectively. A Field test was performed at a suburban site, where the averaged measured k_{OH}' was $17.5 s^{-1}$ with a missing of 20.9% compared to the model simulated result based on measured species. The developed portable LP-FRS instrument expands the measurement capabilities for atmospheric total OH reactivity and will be employed in more field observations.

380 *Author contributions.* BF and WZ designed the research. BF, WZ and NY built the instrument. BF, JL and HZ conducted the instrument test. BF and HZ analysed the data. NW performed the simulation. BF and WZ wrote the paper. YL, ZZ and YL helped the field test. All authors discussed the results and commented on the paper.

Competing interests. The authors declare that they have no conflict of interest.



385

Financial support. This research has been supported by the National Key Research and Development Program of China (grant no. 2022YFC370030401, 2023YFC3705502), the National Natural Science Foundation of China (grant no. U21A2028, 42105099, 91544228), the 2024 Industrialization Fund of Wanjiang Emerging Industry Technology Development Centre (grant no. WJ24CYHXM07) and the HFIPS Director's Fund (grant no. BJPY2023A02, YZJJ202101).

390 **References**

- Atkinson, R., Baulch, D. L., Cox, R. A., Crowley, J. N., Hampson, R. F., Hynes, R. G., Jenkin, M. E., Rossi, M. J., and Troe, J.: Evaluated kinetic and photochemical data for atmospheric chemistry: Volume I - gas phase reactions of O_x, HO_x, NO_x and SO_x species, *Atmos. Chem. Phys.*, 4, 1461-1738, <https://doi.org/10.5194/acp-4-1461-2004>, 2004.
- Atkinson, R., Baulch, D. L., Cox, R. A., Crowley, J. N., Hampson, R. F., Hynes, R. G., Jenkin, M. E., Rossi, M. J., and Troe, J.: Evaluated kinetic and photochemical data for atmospheric chemistry: Volume II - gas phase reactions of organic species, *Atmos. Chem. Phys.*, 6, 3625-4055. <https://doi.org/10.5194/acp-6-3625-2006>, 2006.
- Brecha, R. J., Pedrotti, L. M., and Krause, D.: Magnetic rotation spectroscopy of molecular oxygen with a diode laser, *J. Opt. Soc. Am. B*, 14(8), 1921-1930, <http://doi.org/10.1063/1.1149176>, 1997.
- Cheng, F., Zhao, W., Fang, B., Zhang, Y., Yang, N., Zhou, H., and Zhang, W.: High band-width mid-infrared frequency-modulated Faraday rotation spectrometer for time resolved measurement of the OH radical, *Opt. Express*, 31(15), 25058-25069, <https://doi.org/10.1364/OE.4932702>, 2023.
- Di Carlo, P., Brune, W. H., Martinez, M., Harder, H., Leshner, R., Ren, X., Thornberry, T., Carroll, M. A., Young, V., Shepson, P. B., Riemer, D., Apel, E., and Campbell, C.: Missing OH reactivity in a forest: evidence for unknown reactive biogenic VOCs, *Science*, 304, 722-725, <https://doi.org/10.1126/science.1094392>, 2004.
- Fang, B., Yang, N., Wang, C., Zhao, W., Xu, X., Zhang, Y., and Zhang, W.: Detection of nitric oxide with Faraday rotation spectroscopy at 5.33 μm, *Chin. J. Chem. Phys.*, 33(1), 37-42, <https://doi.org/10.1063/1674-0068/cjcp1910182>, 2020.
- Fatahi, Y., Kouznetsov, R., and Sofiev, M.: The effect of accounting for public holidays on the skills of the atmospheric composition model SILAM v.5.7, *Geosci. Model Dev.*, 14, 7459-7475, <https://doi.org/10.5194/gmd-14-7459-2021>, 2021.
- Fuchs, H., Hofzumahaus, A., Rohrer, F., Bohn, B., Brauers, T., Dorn, H. P., Häsel, R., Holland, F., Kaminski, M., Li, X., Lu, K., Nehr, S., Tillmann, R., Wegener, R., and Wahner, A.: Experimental evidence for efficient hydroxyl radical regeneration in isoprene oxidation, *Nat. Geosci.*, 6, 1023-1026, <https://doi.org/10.1038/ngeo1964>, 2013.
- Fuchs, H., Novelli, A., Rolletter, M., Hofzumahaus, A., Pfannerstill, E. Y., Kessel, S., Edtbauer, A., Williams, J., Michoud, V., Dusanter, S., Locoge, N., Zannoni, N., Gros, V., Truong, F., Sarda-Esteve, R., Cryer, D. R., Brumby, C. A., Whalley, L. K., Stone, D., Seakins, P. W., Heard, D. E., Schoemaeker, C., Blocquet, M., Coudert, S., Batut, S., Fittschen, C., Thames, A. B., Brune, W. H., Ernest, C., Harder, H., Müller, J. B. A., Elste, T., Kubistin, D., Andres, S., Bohn, B., Hohaus, T., Holland, F., Li, X., Rohrer, F., Kiendler-Scharr, A., Tillmann, R., Wegener, R., Yu, Z., Zhou, Q., and



- Wahner, A.: Comparison of OH reactivity measurements in the atmospheric simulation chamber SAPHIR, *Atmos. Meas. Tech.*, 10, 4023-4053, <https://doi.org/10.5194/amt-10-4023-2017>, 2017.
- Goldstein, A. H. and Galbally, I. E.: Known and unexplored organic constituents in the Earth's atmosphere, *Environ. Sci. Technol.*, 41, 1514-1521, <https://doi.org/10.1021/es072476p>, 2007.
- 420 Gordon, I. E., Rothman, L. S., Hargreaves, R. J., Hashemi, R., Karlovets, E. V., Skinner, F. M., Conway, E. K., Hill, C., Kochanov, R. V., Tan, Y., Wcisło, P., Finenko, A. A., Nelson, K., Bernath, P. F., Birk, M., Boudon, V., Campargue, A., Chance, K. V., Coustenis, A., Drouin, B. J., Flaud, J. M., Gamache, R. R., Hodges, J. T., Jacquemart, D., Mlawer, E. J., Nikitin, A. V., Perevalov, V. I., Rotger, M., Tennyson, J., Toon, G. C., Tran, H., Tyuterev, V. G., Adkins, E. M., Baker, A., Barbe, A., Can è E., Cs ász á, A. G., Dudaryonok, A., Egorov, O., Fleisher, A. J., Fleurbaey, H., Foltynowicz, A., Furtenbacher, T., Harrison, J. J., Hartmann, J. M., Horneman, V. M., Huang, X., Karman, T., Karns, J., Kassi, S., Kleiner, I., Kofman, V., Kwabia-Tchana, F., Lavrentieva, N. N., Lee, T. J., Long, D. A., Lukashchuk, A. A., Lyulin, O. M., Makhnev, V. Y., Matt, W., Massie, S. T., Melosso, M., Mikhailenko, S. N., Mondelain, D., Müller, H. S. P., Naumenko, O. V., Perrin, A., Polyansky, O. L., Raddaoui, E., Raston, P. L., Reed, Z. D., Rey, M., Richard, C., T óbi á, R., Sadiék, I., Schwenke, D. W., Starikova, E., Sung, K., Tamassia, F., Tashkun, S. A., Auwera, J. V., Vasilenko, I. A., Viganin, A. A., Villanueva, G. L., Vispoel, B., Wagner, G., Yachmenev, A., and Yurchenko, S. N.: The HITRAN2020 molecular spectroscopic database, *J. Quant. Spectrosc. Radiat. Transfer.*, 277, 107949, <https://doi.org/10.1016/j.jqsrt.2021.107949>, 2022.
- 430 Hansen, R. F., Griffith, S. M., Dusanter, S., Rickly, P. S., Stevens, P. S., Bertman, S. B., Carroll, M. A., Erickson, M. H., Flynn, J. H., Grossberg, N., Jobson, B. T., Lefer, B. L., and Wallace, H. W.: Measurements of total hydroxyl radical reactivity during CABINEX 2009 - Part 1: field measurements, *Atmos. Chem. Phys.*, 14, 2923-2937, <https://doi.org/10.5194/acp-14-2923-2014>, 2014.
- Hansen, R. F., Blocquet, M., Schoemaeker, C., L ónardis, T., Locoge, N., Fittschen, C., Hanoune, B., Stevens, P. S., Sinha, V., and Dusanter, S.: Intercomparison of the comparative reactivity method (CRM) and pump-probe technique for measuring total OH reactivity in an urban environment, *Atmos. Meas. Tech.*, 8, 4243-4264, <https://doi.org/10.5194/amt-8-4243-2015>, 2015.
- 440 Heald, C. L., de Gouw, J., Goldstein, A. H., Guenther, A. B., Hayes, P. L., Hu, W., Isaacman-VanWertz, G., Jimenez, J. L., Keutsch, F. N., Koss, A. R., Misztal, P. K., Rappenglück, B., Roberts, J. M., Stevens, P. S., Washenfelder, R. A., Warneke, C., and Young, C. J.: Contrasting reactive organic carbon observations in the southeast United States (SOAS) and southern California (CalNex), *Environ. Sci. Technol.*, 54, 14923-14935, <https://dx.doi.org/10.1021/acs.est.0c05027>, 2020.
- 445 Hens, K., Novelli, A., Martinez, M., Auld, J., Axinte, R., Bohn, B., Fischer, H., Keronen, P., Kubistin, D., N óscher, A. C., Oswald, R., Paasonen, P., Pet ä T., Regelin, E., Sander, R., Sinha, V., Sipil ä M., Taraborrelli, D., Tatum Ernest, C., Williams, J., Lelieveld, J., and Harder, H.: Observation and modelling of HO_x radicals in a boreal forest, *Atmos. Chem. Phys.*, 14, 8723-8747, <https://doi.org/10.5194/acp-14-8723-2014>, 2014.
- 450



- Hunter, J.F., Day, D. A., Palm, B. B., Yatavelli, R. L. N., Chan, A. W. H., Kaser, L., Cappellin, L., Hayes, P. L., Cross, E. S., Carrasquillo, A. J., Campuzano-Jost, P., Stark, H., Zhao, Y., Hohaus, T., Smith, J. N., Hansel, A., Karl, T., Goldstein, A. H., Guenther, A., Worsnop, D. R., Thornton, J. A., Heald, C. L., Jimenez, J. L., and Kroll, J. H.: Comprehensive characterization of atmospheric organic carbon at a forested site, *Nat. Geosci.*, 10, 748-753, <https://doi.org/10.1038/NGEO3018>, 2017.
- 455
- Ingham, T., Goddard, A., Whalley, L. K., Furneaux, K. L., Edwards, P. M., Seal, C. P., Self, D. E., Johnson, G. P., Read, K. A., Lee, J. D., and Heard, D. E.: A flow-tube based laser-induced fluorescence instrument to measure OH reactivity in the troposphere, *Atmos. Meas. Tech.*, 2, 465-477, <https://doi.org/10.5194/amt-2-465-2009>, 2009.
- Ivanov, A. V., Trakhtenberg, S., Bertram, A. K., Gershenson, Y. M., and Molina, M. J., OH, HO₂, and ozone gaseous diffusion coefficients, *J. Phys. Chem. A*, 111, 1632-1637, <https://doi.org/10.1021/jp066558w>, 2007.
- 460
- Khayyam, J., Xie, P., Xu, J., Tian, X., Feng, H., and Qinjin, W.: Vertically resolved meteorological adjustments of aerosols and trace gases in Beijing, Taiyuan, and Hefei by using RF model, *Sci. Total Environ.*, 948, 174795, <https://doi.org/10.1016/j.scitotenv.2024.174795>, 2024.
- Kim, S., Sanchez, D., Wang, M., Seco, R., Jeong, D., Hughes, S., Barletta, B., Blake, D. R., Jung, J., Kim, D., Lee, G., Lee, M., Ahn, J., Lee, S.-D., Cho, G., Sung, M. Y., Lee, Y. H., Kim, D. B., Kim, Y., Woo, J. H., Jo, D., Park, R., Park, J. H., Hong, Y. D., and Hong, J. H.: OH reactivity in urban and suburban regions in Seoul, South Korea - an East Asian megacity in a rapid transition, *Faraday Discuss.*, 189, 231-251, <https://doi.org/10.1039/C5FD00230C>, 2016.
- 465
- Kohno, N., Zhou, J., Li, J., Takemura, M., Ono, N., Sadanaga, Y., Nakashima, Y., Sato, K., Kato, S., Sakamoto, Y., and Kajii, Y.: Impacts of missing OH reactivity and aerosol uptake of HO₂ radicals on tropospheric O₃ production during the AQUAS-Kyoto summer campaign in 2018, *Atmos. Environ.*, 281, 119130, <https://doi.org/10.1016/j.atmosenv.2022.119130>, 2022.
- 470
- Kovacs, T. A. and Brune, W. H.: Total OH loss rate measurement, *J. Atmos. Chem.*, 39, 105-122, <https://doi.org/10.1023/A:1010614113786>, 2001.
- Kumar, V. and Sinha, V.: VOC-OHM: A new technique for rapid measurements of ambient total OH reactivity and volatile organic compounds using a single proton transfer reaction mass spectrometer, *Int. J. Mass Spectrom.*, 374, 55-63, <https://doi.org/10.1016/j.ijms.2014.10.012>, 2014.
- 475
- Lawrence, M. G.: The relationship between relative humidity and the dewpoint temperature in moist air, *B. Am. Meteorol. Soc.*, 86(2), 225-234, <https://doi.org/10.1175/BAMS-86-2-225>, 2005.
- Lewicki, R., Doty III, J. H., Curl, R. F., Tittel, F. K., and Wysocki, G.: Ultrasensitive detection of nitric oxide at 5.33 μm by using external cavity quantum cascade laser-based Faraday rotation spectroscopy, *P. Natl. Acad. Sci. USA*, 106(31), 12587-12592, <https://doi.org/10.1073/pnas.0906291106>, 2009.
- 480
- Lewis, T., Heard, D. E., and Blitz, M. A.: A novel multiplex absorption spectrometer for time-resolved studies, *Rev. Sci. Instrum.*, 89, 024101, <https://doi.org/10.1063/1.5006539>, 2018.



- Li, J., Kohno, N., Sakamoto, Y., Fukusaki, Y., Kousa, Y., Sadanaga, Y., Nakashima, Y., Sato, K., Ramasamy, S., Takami, A.,
485 Yoshino, A., Nakayama, T., Kato, S., Ono, N., Zhou, J., Bai, Y., and Kajii, Y.: A quantitative understanding of total OH
reactivity and ozone production in a coastal industrial area during the Yokohama air quality study (AQUAS) campaign
of summer 2019, *Atmos. Environ.*, 267, 118754, <https://doi.org/10.1016/j.atmosenv.2021.118754>, 2021.
- Li, J., Kohno, N., Sakamoto, Y., Pham, H. G., Murano, K., Sato, K., Nakayama, T., and Kajii, Y.: Potential factors
490 contributing to ozone production in AQUAS-Kyoto campaign in summer 2020: natural source-related missing OH
reactivity and heterogeneous HO₂/RO₂ loss, *Environ. Sci. Technol.*, 56, 12926-12936,
<https://doi.org/10.1021/acs.est.2c03628>, 2022.
- Litfin, G., Pollock, C. R., Curl, R. F., Tittel, F.K.: Sensitivity enhancement of laser absorption spectroscopy by magnetic
rotation effect, *J. Chem. Phys.*, 72, 6602-6605, <https://doi.org/10.1063/1.439117>, 1980.
- Liu, Y., Ivanov, A. V., and Molina, M. J.: Temperature dependence of OH diffusion in air and He, *Geophys. Res. Lett.*, 36,
495 L03816, <https://doi.org/10.1029/2008GL036170>, 2009.
- Lu, K., Guo, S., Tan, Z., Wang, H., Shang, D., Liu, Y., Li, X., Wu, Z., Hu, M., and Zhang, Y.: Exploring atmospheric free-
radical chemistry in China: the self-cleansing capacity and the formation of secondary air pollution, *Natl. Sci. Rev.*, 6(3),
579-594, <https://doi.org/10.1093/nsr/nwy073>, 2018.
- Lou, S., Holland, F., Rohrer, F., Lu, K., Bohn, B., Brauers, T., Chang, C. C., Fuchs, H., Häsel, R., Kita, K., Kondo, Y., Li,
500 X., Shao, M., Zeng, L., Wahner, A., Zhang, Y., Wang, W., and Hofzumahaus, A.: Atmospheric OH reactivities in the
Pearl River Delta - China in summer 2006: measurement and model results, *Atmos. Chem. Phys.*, 10, 11243-11260,
<https://doi.org/10.5194/acp-10-11243-2010>, 2010.
- Luo, P., Chung, C., and Lee, Y.: Rate coefficient of the reaction CH₂OO + NO₂ probed with a quantum-cascade laser near 11
µm, *Phys. Chem. Chem. Phys.*, 21, 17578-17583, <https://doi.org/10.1039/C9CP03333E>, 2019.
- 505 Luo, P.: Long-wave mid-infrared time-resolved dual-comb spectroscopy of short-lived intermediates, *Opt. Lett.*, 45(24),
6791-6794, <https://doi.org/10.1364/OL.413754>, 2020.
- Luo, P. and Horng, E.: Simultaneous determination of transient free radicals and reaction kinetics by high-resolution time-
resolved dual-comb spectroscopy, *Commun. Chem.*, 3, 95, <https://doi.org/10.1038/s42004-020-00353-6>, 2020.
- Mao, J., Ren, X., Brune, W. H., Olson, J. R., Crawford, J. H., Fried, A., Huey, L. G., Cohen, R. C., Heikes, B., Singh, H. B.,
510 Blake, D. R., Sachse, G. W., Diskin, G. S., Hall, S. R., and Shetter, R. E.: Airborne measurement of OH reactivity during
INTEX-B, *Atmos. Chem. Phys.*, 9, 163-173, <https://doi.org/10.5194/acp-9-163-2009>, 2009.
- Mao, J., Ren, X., Chen, S., Brune, W., Chen, Z., Martinez, M., Harder, H., Lefter, B., Rappenglück, B., Flynn, J., and
Leuchner, M.: Atmospheric oxidation capacity in the summer of Houston 2006: comparison with summer measurements
in other metropolitan studies, *Atmos. Environ.*, 44, 4107-4115, <https://doi.org/10.1016/j.atmosenv.2009.01.013>, 2010.
- 515 Martinez, M., Harder, H., Kovacs, T. A., Simpas, J. B., Bassis, J., Leshner, R., Brune, W. H., Frost, G. J., Williams, E. J.,
Stroud, C. A., Jobson, B. T., Roberts, J. M., Hall, S. R., Shetter, R. E., Wert, B., Fried, A., Alicke, B., Stutz, J., Young, V.



- L., White, A. B., and Zamora, R. J.: OH and HO₂ concentrations, sources, and loss rates during the Southern Oxidants Study in Nashville, Tennessee, summer 1999, *J. Geophys. Res.*, 108, 4617, <https://doi.org/10.1029/2003JD003551>, 2003.
- 520 Michoud, V., Hansen, R. F., Locoge, N., Stevens, P. S., and Dusanter, S.: Detailed characterizations of the new Mines Douai comparative reactivity method instrument via laboratory experiments and modeling, *Atmos. Meas. Tech.*, 8, 3537-3553, <https://doi.org/10.5194/amt-8-3537-2015>, 2015.
- Muller, J. B. A., Elste, T., Plass-Dülmer, C., Stange, G., Holla, R., Claude, A., Englert, J., Gilge, S., and Kubistin, D.: A novel semi-direct method to measure OH reactivity by chemical ionisation mass spectrometry (CIMS), *Atmos. Meas. Tech.*, 11, 4413-4433, <https://doi.org/10.5194/amt-11-4413-2018>, 2018.
- 525 Nicely, J. M., Canty, T. P., Manyin, M., Oman, L. D., Salawitch, R. J., Steenrod, S. D., Strahan, S. E., and Strode, S. A.: Changes in Global Tropospheric OH Expected as a Result of Climate Change Over the Last Several Decades, *J. Geophys. Res-Atmos.*, 123, 10774-10795, <https://doi.org/10.1029/2018JD028388>, 2018.
- Nödscher, A. C., Sinha, V., Bockisch, S., Klöpfel, T., and Williams, J.: Total OH reactivity measurements using a new fast Gas Chromatographic Photo-Ionization Detector (GC-PID), *Atmos. Meas. Tech.*, 5, 2981-2992,
530 <https://doi.org/10.5194/amt-5-2981-2012>, 2012.
- Parker, A. E., Amedro, D., Schoemaeker, C., and Fittschen, C.: OH radical reactivity measurements by FAGE, *Environ. Eng. Manage. J.*, 10, 107-114, 2011.
- Pilgrim, J. S., Jennings, R. T., and Taatjes, C. A.: Temperature controlled multiple pass absorption cell for gas phase chemical kinetics studies, *Rev. Sci. Instrum.*, 68, 1875-1878, <https://doi.org/10.1063/1.11479601>, 1997.
- 535 Praplan, A. P., Pfannerstill, E., Williams, J., and Helen, H.: OH reactivity of the urban air in Helsinki, Finland, during winter, *Atmos. Environ.*, 169, 150-161, <https://doi.org/10.1016/j.atmosenv.2017.09.013>, 2017.
- Qian, H., Turton, D., Seakins, P. W., and Pilling, M. J.: Dynamic frequency stabilization of infrared diode laser for kinetic studies, *Chem. Phys. Lett.*, 322, 57-64, [https://doi.org/10.1016/S0009-2614\(00\)00395-X](https://doi.org/10.1016/S0009-2614(00)00395-X), 2000.
- Sadanaga, Y., Yoshino, A., Watanabe, K., Yoshioka, A., Wakazono, Y., Kanaya, Y., and Kajii, Y.: Development of a measurement system of OH reactivity in the atmosphere by using a laser-induced pump and probe technique, *Rev. Sci. Instrum.*, 75, 2648-2655, <https://doi.org/10.1063/1.1775311>, 2004.
- 540 Safieddine, S. A., Heald, C. L., and Henderson, B. H.: The global nonmethane reactive organic carbon budget: A modeling perspective, *Geophys. Res. Lett.*, 44, 3897-3906, <https://doi.org/10.1002/2017GL072602>, 2017.
- Schilt, S., Thévenaz, L., and Robert, P.: Wavelength modulation spectroscopy: combined frequency and intensity laser modulation, *Appl. Opt.*, 42(33), 6728-6738, <https://doi.org/10.1364/AO.42.006728>, 2003.
- 545 Sinha, V., Williams, J., Crowley, J. N., and Lelieveld, J.: The Comparative Reactivity Method - a new tool to measure total OH Reactivity in ambient air, *Atmos. Chem. Phys.*, 8, 2213-2227, <https://doi.org/10.5194/acp-8-2213-2008>, 2008.
- Sinha, V., Williams, J., Diesch, J. M., Drewnick, F., Martinez, M., Harder, H., Regelin, E., Kubistin, D., Bozem, H., HosaynaliBeygi, Z., Fischer, H., Andrés-Hernández, M. D., Kartal, D., Adame, J. A., and Lelieveld, J.: Constraints on



- 550 instantaneous ozone production rates and regimes during DOMINO derived using in-situ OH reactivity measurements, *Atmos. Chem. Phys.*, 12, 7269-7283, <https://doi.org/10.5194/acp-12-7269-2012>, 2012.
- Song, B., Yan, X., Tan, S., Sai, B., Lai, S., Yu, H., Ou, C., and Lu, X.: Human mobility models reveal the underlying mechanism of seasonal movements across China, *Int. J. Mod. Phys. C*, 33(04), 2250054, <https://doi.org/10.1142/S0129183122500541>, 2022.
- 555 Stone, D., Whalley, L. K., and Heard, D. E.: Tropospheric OH and HO₂ radicals: field measurements and model comparisons, *Chem. Soc. Rev.*, 41, 6348-6404, <https://doi.org/10.1039/c2cs35140d>, 2012.
- Stone, D., Whalley, L. K., Ingham, T., Edwards, P. M., Cryer, D. R., Brumby, C. A., Seakins, P. W., and Heard, D. E.: Measurement of OH reactivity by laser flash photolysis coupled with laser-induced fluorescence spectroscopy, *Atmos. Meas. Tech.*, 9, 2827-2844, <https://doi.org/10.5194/amt-9-2827-2016>, 2016.
- 560 Teng, C. C., Yan, C., Rousso, A., Zhong, H., Chen, T., Zhang, E. J., Ju, Y., and Wysocki, G.: Time-resolved HO₂ detection with Faraday rotation spectroscopy in a photolysis reactor, *Opt. Express*, 29(2), 2769-2779, <https://doi.org/10.1364/OE.413063>, 2021.
- Trutna, W. R. and Byer, R. L.: Multiple-pass Raman gain cell, *Appl. Opt.*, 19(2), 301-312, <https://doi.org/10.1364/AO.19.000301>, 1980.
- 565 Wang, W., Li, X., Cheng, Y., Parrish, D. D., Ni, R., Tan, Z., Liu, Y., Lu, S., Wu, Y., Chen, S., Lu, K., Hu, M., Zeng, L., Shao, M., Huang, C., Tian, X., Leung, K. M., Chen, L., Fan, M., Zhang, Q., Rohrer, F., Wahner, A., Pöschl, U., Su, H., and Zhang, Y.: Ozone pollution mitigation strategy informed by long-term trends of atmospheric oxidation capacity, *Nat. Geosci.*, 17, 20-25, <https://doi.org/10.1038/s41561-023-01334-9>, 2023.
- Wei, N., Fang, B., Zhao, W., Wang, C., Yang, N., Zhang, W., Chen, W., and Fittschen, C.: Time-resolved laser-flash photolysis Faraday rotation spectrometer: a new tool for total OH reactivity measurement and free radical kinetics research, *Anal. Chem.*, 92, 4334-4339, <https://doi.org/10.1021/acs.analchem.9b05117>, 2020.
- 570 Wei, N., Zhao, W., Yao, Y., Wang, H., Liu, Z., Xu, X., Rahman, M., Zhang, C., Fittschen, C., and Zhang, W.: Peroxy radical chemistry during ozone photochemical pollution season at a suburban site in the boundary of Jiangsu-Anhui-Shandong-Henan region, China, *Sci. Total Environ.*, 904, 166355, <https://doi.org/10.1016/j.scitotenv.2023.166355>, 2023.
- 575 Westberg, J. and Axner, O.: Lineshape asymmetries in Faraday modulation spectroscopy, *Appl. Phys. B*, 116, 467-476, <https://link.springer.com/article/10.1007/s00340-013-5721-x>, 2014.
- Wolfe, G. M., Marvin, M. R., Roberts, S. J., Travis, K. R., and Liao, J.: The framework for 0-D atmospheric modeling (F0AM) v3.1, *Geosci. Model Dev.*, 9, 3309-3319, <https://doi.org/10.5194/gmd-9-3309-2016>, 2016.
- 580 Yan, C., Teng, C. C., Chen, T., Zhong, H., Rousso, A., Zhao, H., Ma, G., Wysocki, G., and Ju, Y.: The kinetic study of excited singlet oxygen atom O(¹D) reactions with acetylene, *Combust. Flame*, 212, 135-141, <https://doi.org/10.1016/j.combustflame.2019.10.034>, 2020.



- Yang, Y., Shao, M., Wang, X., Nödscher, A. C., Kessel, S., Guenther, A., and Williams, J.: Towards a quantitative understanding of total OH reactivity: A review, *Atmos. Environ.*, 134, 147-161, <http://dx.doi.org/10.1016/j.atmosenv.2016.03.010>, 2016.
- 585 Yang, Y., Shao, M., Keßel, S., Li, Y., Lu, K., Lu, S., Williams, J., Zhang, Y., Zeng, L., Nödscher, A. C., Wu, Y., Wang, X., and Zheng, J.: How the OH reactivity affects the ozone production efficiency: case studies in Beijing and Heshan, China, *Atmos. Chem. Phys.*, 17, 7127-7142, <https://doi.org/10.5194/acp-17-7127-2017>, 2017.
- Zannoni, N., Dusanter, S., Gros, V., Sarda Esteve, R., Michoud, V., Sinha, V., Locoge, N., and Bonsang, B.: Intercomparison of two comparative reactivity method instruments in the Mediterranean basin during summer 2013, *Atmos. Meas. Tech.*, 8, 3851-3865, <https://doi.org/10.5194/amt-8-3851-2015>, 2015.
- 590 Zhao, W., Wysocki, G., Chen, W., Fertein, E., Coq, L. D., Petiprez, D., and Zhang, W.: Sensitive and selective detection of OH radicals using Faraday rotation spectroscopy at 2.8 μm , *Opt. Express*, 19(3), 2493-2501, <https://doi.org/10.1364/OE.19.002493>, 2011.
- Zhao, W., Wysoki, G., Chen, W., Zhang, W.: High sensitivity Faraday rotation spectrometer for hydroxyl radical detection at 2.8 μm , *Appl. Phys. B*, 109, 511-519, <https://doi.org/10.1007/s00340-012-5089-3>, 2012.
- 595 Zhao, W., Fang, B., Lin, X., Gai, Y., Zhang, W., Chen, W., Chen, Z., Zhang, H., and Chen, W.: Superconducting-magnet-based Faraday rotation spectrometer for real time in situ measurement of OH radicals at 106 molecule/cm³ level in an atmospheric simulation chamber, *Anal. Chem.*, 90, 3958-3964, <https://doi.org/10.1021/acs.analchem.7b04949>, 2018.